Article

# Antarctic calving loss rivals ice-shelf thinning

https://doi.org/10.1038/s41586-022-05037-w

Received: 21 January 2022

Accepted: 28 June 2022

Published online: 10 August 2022

Check for updates

Chad A. Greene[1]✉, Alex S. Gardner[1], Nicole-Jeanne Schlegel[1] & Alexander D. Fraser[2]

Antarctica's ice shelves help to control the flow of glacial ice as it drains into the ocean, meaning that the rate of global sea-level rise is subject to the structural integrity of these fragile, floating extensions of the ice sheet[1–3]. Until now, data limitations have made it difficult to monitor the growth and retreat cycles of ice shelves on a large scale, and the full impact of recent calving-front changes on ice-shelf buttressing has not been understood. Here, by combining data from multiple optical and radar satellite sensors, we generate pan-Antarctic, spatially continuous coastlines at roughly annual resolution since 1997. We show that from 1997 to 2021, Antarctica experienced a net loss of 36,701 ± 1,465 square kilometres (1.9 per cent) of ice-shelf area that cannot be fully regained before the next series of major calving events, which are likely to occur in the next decade. Mass loss associated with ice-front retreat (5,874 ± 396 gigatonnes) has been approximately equal to mass change owing to ice-shelf thinning over the past quarter of a century (6,113 ± 452 gigatonnes), meaning that the total mass loss is nearly double that which could be measured by altimetry-based surveys alone. We model the impacts of Antarctica's recent coastline evolution in the absence of additional feedbacks, and find that calving and thinning have produced equivalent reductions in ice-shelf buttressing since 2007, and that further retreat could produce increasingly significant sea-level rise in the future.

Ice shelves serve a vital role in preventing the rapid collapse of the Antarctic Ice Sheet[1], and, accordingly, the rate of global sea-level rise can be influenced by any process that affects the thickness or form of ice-shelf extents[2,3]. As the climate warms, Antarctic surface melt is expected to increase along the periphery and potentially lead to rheological weakening[4], hydrofracture[5], and the partial or wholesale collapse of ice shelves around the continent[6–8]. Grounded glaciers are primed to accelerate in response to ice-shelf loss[9], and although the theory of marine ice-cliff instability is hotly debated[10–13], an essential element of the hypothesis requires sudden, catastrophic calving events to set off a domino effect that could result in large-scale ice-sheet destabilization[14]. Beyond their significance to rapid sea-level rise, major calving events can radically alter polynya activity[15], oceanic water-mass formation[16], primary productivity[15,17] and the circulation of the Southern Ocean[18–21], while fundamentally reshaping marine ecosystems, as vast underwater regions become suddenly exposed to sunlight and atmospheric exchange[17,22].

Satellite altimeters have enabled decades of observation of melt-driven ice-shelf mass loss[23], but mass changes associated with Antarctica's coastal evolution have seen less attention on a large scale, owing to a sparsity of satellites observations, from which it can be difficult to manually or automatically distinguish glacier ice from icebergs and sea ice[24]. Where coastline changes have been observed, periods of retreat have been linked to regional increases in sea surface temperatures or a reduction in sea ice[25–27], but on a pan-Antarctic scale, no clear or consistent trends in coastal evolution have previously been reported.

## Antarctica's evolving coastline

We combined data from multiple optical-band, thermal-band and radar satellite sensors, acquired roughly annually from 1997 to 2021, then constrained manual coastline delineations to be consistent with observations of ice flow (Methods). The resulting coastline evolution data product shown in Fig. 1, Extended Data Fig. 1, Supplementary Information and the Supplementary Videos provides a clear picture of how each of Antarctica's ice shelves have advanced or retreated over the past quarter of a century.

Figure 2 shows that since 1997, 118 ice shelves have retreated by a gross 54,029 ± 634 km$^2$, which has been partially offset by gains from 63 ice shelves that advanced by 17,781 ± 438 km$^2$. The net result is a loss of 36,701 ± 1,465 km$^2$ including 454 ± 1,245 km$^2$ retreat of grounded termini and glaciers that flow into unnamed ice shelves (Supplementary Table 1). A close look at the coastline evolution of individual ice shelves (Fig. 1, Extended Data Fig. 1 and Supplementary Information) reveals a diverse pattern of behaviours taking place around the continent, including evidence[28] of rifting (for example, Ronne and Larsen C), edge wasting (for example, Totten), rapid disintegration (for example, Larsen A, Larsen B and Wilkins), steady advance (for example, Filchner and Cook), and repeated cycles of advance and calving (for example, Ninnis).

During the period of study, ice-shelf area losses were led by major calving events of large, tabular bergs shed from the Ross and Ronne ice shelves in 2000[29], and again from the Ross Ice Shelf in 2002[30] (Fig. 2). To be clear, the calving behaviour of the Ross and Ronne ice shelves

[1]Jet Propulsion Laboratory, California Institute of Technology, Pasadena, CA, USA. [2]Australian Antarctic Program Partnership, Institute for Marine and Antarctic Studies, University of Tasmania, Hobart, Tasmania, Australia. ✉e-mail: chad@chadagreene.com

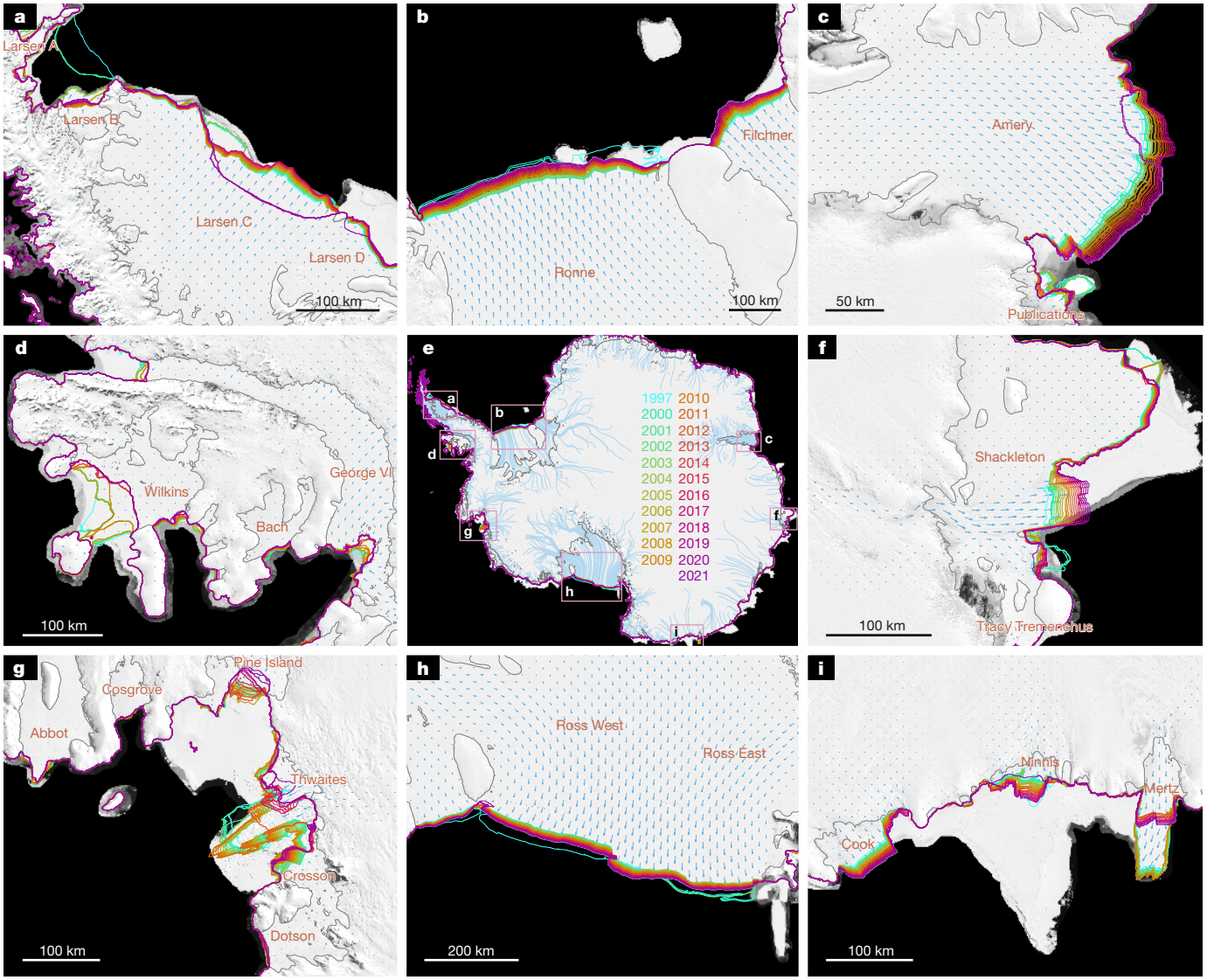


**Fig. 1 | Antarctic coastal change since 1997. a**,**d**, The Larsen (**a**) and Wilkins (**d**) ice shelves of the Antarctic Peninsula have retreated in a stair-step series of events over the past quarter of a century. **b**,**h**, Antarctica's largest ice shelves Ronne (**b**) and Ross (**h**) experienced major calving events in 2000 and 2002 and have since steadily advanced until the May 2021 calving of iceberg A76, not shown here. **g**, Thwaites Glacier is perhaps the most difficult coastline to track, as its thick and broken iceberg tongue remained semi-connected to the ice shelf for several years. **i**, A sequence of events is seen at Mertz Glacier Tongue, whose tip touched ground on the western side[48], pushing the tongue to the east until the tip broke off in 2010, and the ice shelf has been advancing towards the west again ever since. Meanwhile, nearby Cook Ice Shelf has steadily advanced throughout the entire period of observation. Panels **c**, **e** and **f** show the Amery Ice Shelf, a map indicating the locations of insets, and Shackleton Ice Shelf, respectively.

is naturally cyclic on multidecadal timescales, and there is no indication that either ice shelf exhibited any abnormal behaviour during our observations. After the last in the series of major calving events in 2002, Antarctica's overall ice-shelf area has remained relatively steady or trended slightly upwards at times, possibly giving the impression of an ice sheet in a state of recovery. However, we find that during the past two decades, steady growth from Antarctica's largest ice shelves has helped mask losses that have occurred elsewhere around the continent. Using a least-squares fit, we find that Antarctica has gained area at a rate of 350 $km^2\ yr^{-1}$ since 2002, and at this rate it would take about 100 years to recover to the total area observed in 1997. An examination of the timing of major calving events from the Ross, Ronne, Filchner and Amery ice shelves suggests that they could all experience major calving events by the end of the 2030s, which would cause further reductions in area well before the ice sheet has had a chance to recover to its 1997 extent (Figs. 2 and 3). We caution that the exact timing of future calving events cannot be predicted from past behaviour; yet, a full recovery of Antarctic ice-shelf area appears unlikely within any plausible range of timing for the next major calving events.

We translate our observations of ice-sheet-area evolution into mass-flux anomalies by multiplying the area of each 240 × 240 m pixel in our time-evolving gridded ice mask by a static ice-shelf thickness grid and an assumed ice density of 917 $kg\ m^{-3}$ (Methods). For calving-flux estimates, we neglect temporal variability in ice-shelf thickness, as melt rates are expected to have minimal effect on ice-shelf thickness, particularly near the ocean, where calving rates are calculated. Along the minimum observed extents of the ice sheet, we find a steady-state calving flux of 1,411 ± 28 Gt $yr^{-1}$, which falls between estimates from two previous studies that used a similar steady-state technique[31,32], but is notably higher than estimates that have relied on detecting and counting discrete calving events[33,34].

Deviations from the steady-state calving rate of each ice shelf are calculated from temporal variations in its total mass, taken as the sum of the thickness of all of its ice pixels for a given time, multiplied by the

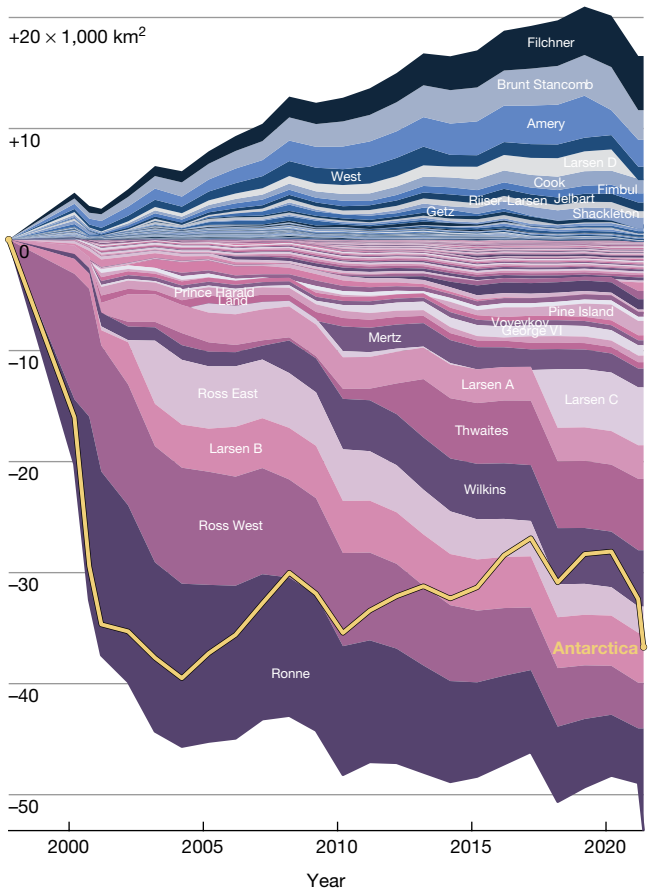


**Fig. 2 | Cumulative area change since 1997.** Among Antarctica's 181 ice shelves surveyed in this study, 118 (shown in pink/purple tones) have lost a total of 54,029 ± 634 km² since 1997, whereas only 63 ice shelves (shown in blue tones) grew in extent by 17,781 ± 438 km². The Ronne and Ross ice shelves together account for 29% of gross losses (15,678 ± 263 km²), and the Filchner and Amery ice shelves together account for 41% of gross gains (7,303 ± 139 km²). The gold line shows a net loss of 36,701 ± 1,465 km² for all of Antarctica, including 454 ± 1,245 km² loss from coastal areas that do not terminate in named ice shelves. It is noted that ice-shelf area anomalies correspond to their visible areas rather than distance from the zero axis, so the downward shifts seen in many ice shelves towards the lower end of the figure in 2010 and 2017 correspond to major calving events at Mertz and Larsen C, respectively. Also, it is noted that the relative influence of the largest outliers such as the Ronne, Ross West and Filchner ice shelves can be effectively removed by ignoring them when visually inspecting this figure.

pixel area and the density of ice (Methods). The results (Supplementary Table 1) show that since 1997, Antarctica has experienced a net loss of 5,874 ± 396 Gt of ice owing to calving. The most significant losses have come from the Ronne Ice Shelf (−2,034 ± 189 Gt) and Thwaites Glacier (−1,968 ± 122 Gt), followed by Larsen C Ice Shelf (−1,167 ± 138 Gt), whose mass loss is primarily attributable to the July 2017 calving of iceberg A68, and the Western Ross Ice Shelf (−930 ± 131 Gt), which has yet to fully recover from calving events that occurred there in March and April 2000. The largest mass gains that occurred during our period of study came from Filchner Ice Shelf (+1,796 ± 71 Gt), whose last major calving event occurred in 1986[35] (Fig. 3).

For context, we compare calving-related mass changes to mass changes caused by ice-shelf thinning or thickening over the same period. From radar altimetry[36] (Methods), we find that within the minimum observed areal extents of the ice sheet, Antarctic ice shelves have lost a net of 6,113 ± 452 Gt of ice owing to thinning. Trends in mass loss were most significant at Getz Ice Shelf (−57.1 ± 0.6 Gt yr$^{-1}$) and the Shackleton Ice Shelf fed by Denman Glacier (−22.7 ± 0.5 Gt), followed by several ice shelves that are all located in the Amundsen Sea or Bellingshausen Sea embayments. When comparing calving-related mass changes to thinning-related changes (Extended Data Fig. 2), we find that the mass balance of most ice shelves is driven more by calving-front processes than by the thickness trends that are commonly associated with anomalies in basal melt. The change in mass of Filchner Ice Shelf has been driven almost entirely by its steady advance, whereas the Ronne, Thwaites, Ross and Wilkins ice shelves have each lost more mass to ice-front retreat than to thinning. The Shackleton Ice Shelf meanwhile experienced substantial losses to thinning, but its net change in mass has been minimal owing to gains in areal extent. In our pan-Antarctic survey, Getz Ice Shelf stands out for experiencing significant losses driven almost entirely by ice-shelf thinning.

## Impacts of changing ice-shelf geometry

We use the Ice-sheet and Sea-level System Model (ISSM)[37] version 4.19 to investigate how observed changes in ice-shelf thickness and calving-front location may have impacted the flow of Antarctica's grounded ice since the 1990s. We use a simple instantaneous-response approach that calculates the change in the ice sheet's stress balance in response to an instantaneous change in ice-shelf area or ice-shelf thickness. Our approach does not consider the effects of time-evolving feedbacks, such as grounding-line migration or changes in grounded-ice geometry, but closely mimics previous studies of grounding-line-flux sensitivity to thinning and calving[2,3,38–42]. To best capture the effects of small, annual changes to the calving front, we use a 20-million-element two-dimensional model mesh with a dense, 100-m spatial resolution in areas that advanced or retreated during the observation period, and coarser resolution farther from the coast (Methods). The model is initialized with velocity and thickness observations collected primarily in the early 2010s, which we extend to the maximum observed extents of the ice sheet where necessary (Methods). We then use data assimilation techniques to best match the observed surface velocities over grounded and floating ice, after the methods described in ref. [42]. For each model experiment simulation, we alter the ice mask or the floating ice thickness, and then solve a stress-balance equation to calculate the instantaneous velocity response to the ascribed perturbation (Methods). From any change in the modelled velocity field, we calculate change in grounding-line flux as a measure of the instantaneous change in buttressing that occurs when the ice-shelf geometry is altered.

The simulation results show a nearly linear increase in instantaneous grounding-line flux each year (Fig. 4a) in response to the range of ice-shelf thicknesses observed from 1992 to 2017. Around Antarctica, the overall rate of thinning has been approximately linear over time throughout the satellite record[23], and our modelled grounding-line flux responds approximately linearly to the forcing, as expected. In agreement with previous modelling studies[38] and observations, our model shows a roughly linear velocity response to recent ice-shelf thickness changes, focused primarily in the rapidly changing West Antarctic, lending credence to the instantaneous-response model as an effective tool for studying perturbations in ice-shelf geometry.

In addition to testing the effects of ice-shelf thinning, we model the effects of changes in buttressing that result from observed changes in calving-front geometry. We find that for the first decade of observations, calving-front evolution probably had little impact on buttressing (Fig. 4b), but since 2007, the modelled response to changes in calving-front extent has increased at approximately the same rate as the modelled increase owing to ice-shelf thinning. The implication is that although the most significant reductions in ice-shelf area came from the Ronne and Ross ice shelves in 2000 and 2002, the calving of these large, tabular bergs had minimal impact on buttressing[3]. For the past decade and a half, however, the model response suggests that smaller, successive ice-shelf-area reductions elsewhere around the continent

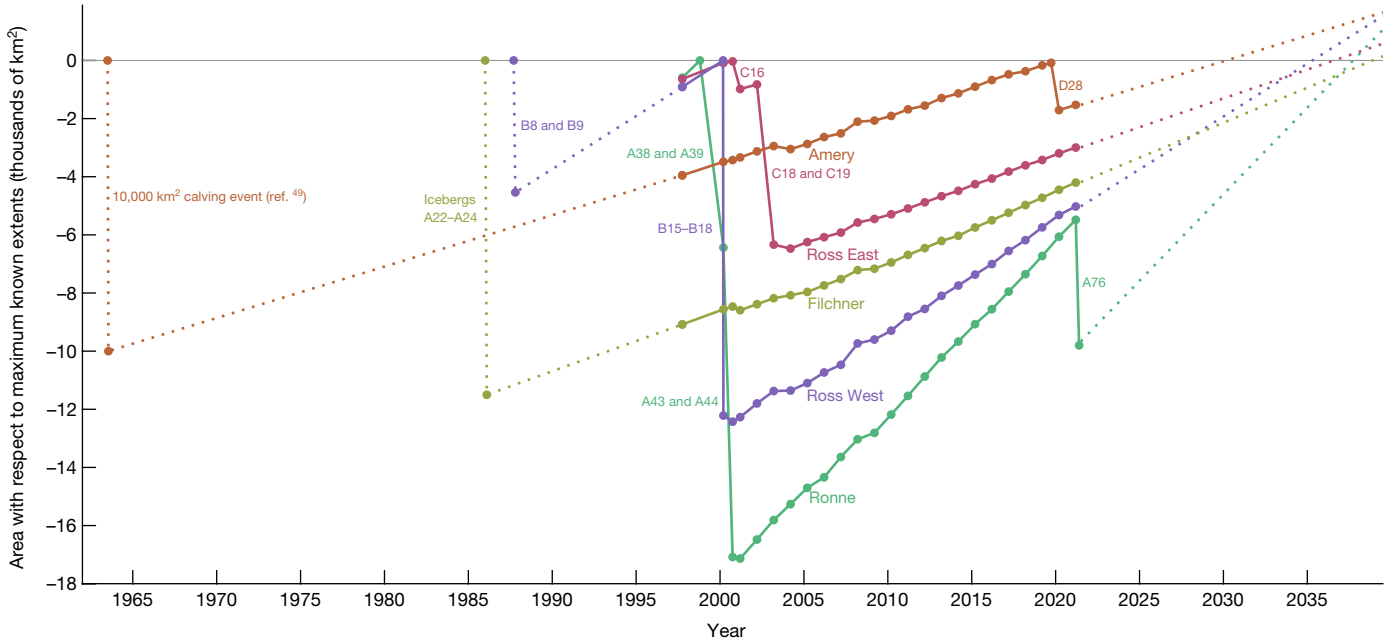


**Fig. 3 | Calving history of Antarctica's largest ice shelves.** Ice-shelf areas are shown relative to their extents just before the largest known calving events for each ice shelf. The solid lines connect observations presented in this study, and the dotted lines extend observed growth rates back in time to known calving events and forwards in time to indicate how long it may take for each ice shelf to reach the extent corresponding to its last major calving event. At Amery Ice Shelf, we measure a growth rate of 177 km$^2$ yr$^{-1}$ from 1997 to 2019 and extrapolate it back to 1963, when a large 10,000 km$^2$ calving event occurred[49]. Amery's history suggests the 2019 calving of iceberg D28 (ref. [50]) occurred as the ice shelf neared its 1963 extent, and extrapolation into the future suggests another calving event may occur at Amery by about 2030. Similarly, a constant growth rate of 220 km$^2$ yr$^{-1}$ since the Filchner Ice Shelf calved 11,500 km$^2$ in 1986 (ref. [35]) suggests that Filchner may be due for another major event in or before the mid 2030s. Unless Antarctica's largest ice shelves grow beyond their maximum known extents, we expect that the Amery, Ross, Filchner and Ronne ice shelves will all experience major calving events in the 2030s or before.

may have cut into more critically important ice, particularly at Pine Island and Thwaites glaciers.

To examine the full range of possible impacts of future ice-shelf degradation, we separately model the instantaneous response to thinning and calving, each in 1% increments of reduction from present-day geometry to total ice-shelf loss (Fig. 4c,d). Thinning was applied to each node as a percentage of the present-day thickness that was used for model initialization, and calving was applied incrementally by removing the nodes closest to the calving front of the previous iteration (Supplementary Videos) and replacing them with the appropriate backstress applied by seawater. Although the modelled response to thinning has been approximately linear for the past few decades of observation, the concavity of the thinning response curves in Fig. 4c suggests that sensitivity to thinning grows slightly more pronounced as ice shelves become thinner. The concavity of the calving-response curves in Fig. 4d is particularly strong, reaffirming that calving can have increasingly large impacts on buttressing as an ice front retreats towards the grounding line. In nature, ice-shelf thinning and calving are not entirely separable, as one can lead to the other, and they are often driven by the same regional influences; yet, we separate the two processes here to identify their relative importance and to better understand such phenomena as thinning in the absence of major calving events, or hydrofracture-driven ice-shelf collapse, which does not strictly require prior thinning[43].

Our model results show that among all of the ice shelves in Antarctica, Pine Island and Thwaites have responded the most strongly to reduced buttressing caused by ice-shelf thinning and calving, the effects of which are well documented in observations[40,41]. Setting aside for a moment the susceptibility of glaciers in the Amundsen Sea Embayment to marine ice-sheet instability, Fig. 4e highlights the role that many of Antarctica's less expressive ice shelves currently play in preventing rapid sea-level rise. Whereas the complete collapse of the Pine Island or Thwaites ice shelves each produce a modelled instantaneous response of less than 50 Gt yr$^{-1}$, the collapse of the Ronne and Filchner ice shelves show an instantaneous increase of 876 Gt yr$^{-1}$ and 272 Gt yr$^{-1}$, respectively. Another compelling example is seen at Moscow University Ice Shelf, whose modelled present-day flow rate (52 Gt yr$^{-1}$) is about half that of Ross East (98 Gt yr$^{-1}$), but if the tightly embayed and intensely buttressed Moscow University Ice Shelf were to suddenly collapse, its grounded ice would accelerate by 121 Gt yr$^{-1}$, whereas the same fate suffered by Ross East causes a modelled increase of only 87 Gt yr$^{-1}$. It should be noted that there is no evidence that the Ross, Ronne, Filchner or Moscow University ice shelves are under any imminent threat of collapse, but we mention them here only to reaffirm their previously reported role[39,42] in holding back a rapid influx of glacial ice into the ocean.

## Outlook for the future

We model the isolated impacts of observed changes in ice-shelf geometry to understand the relative influence that calving and thinning can each have on grounded glacier flow. Our approach only accounts for instantaneous changes in stress balance, and does not explore time-evolving ice-sheet responses or any transient feedbacks that are known to cause further impacts on ice flow[39,42,44]. For example, ice-shelf thinning often leads to grounding-line retreat[45], which itself can increase grounding-line flux[46]; calving can reshape an ocean environment and influence melt rates[21]; and increased melt can lead to a weakened ice shelf that is more susceptible to calving or collapse[8,9]. Accordingly, the modelled sensitivities we present offer a narrow but insightful[2,3,38,40,41] view of how the buttressing strength of ice shelves may be compromised owing to thinning or calving, when each process is considered in isolation.

We know that ice-shelf thinning tends to occur slowly over time, and can only impact buttressing within a limited range on decadal timescales. By comparison, calving and ice-shelf collapse can occur

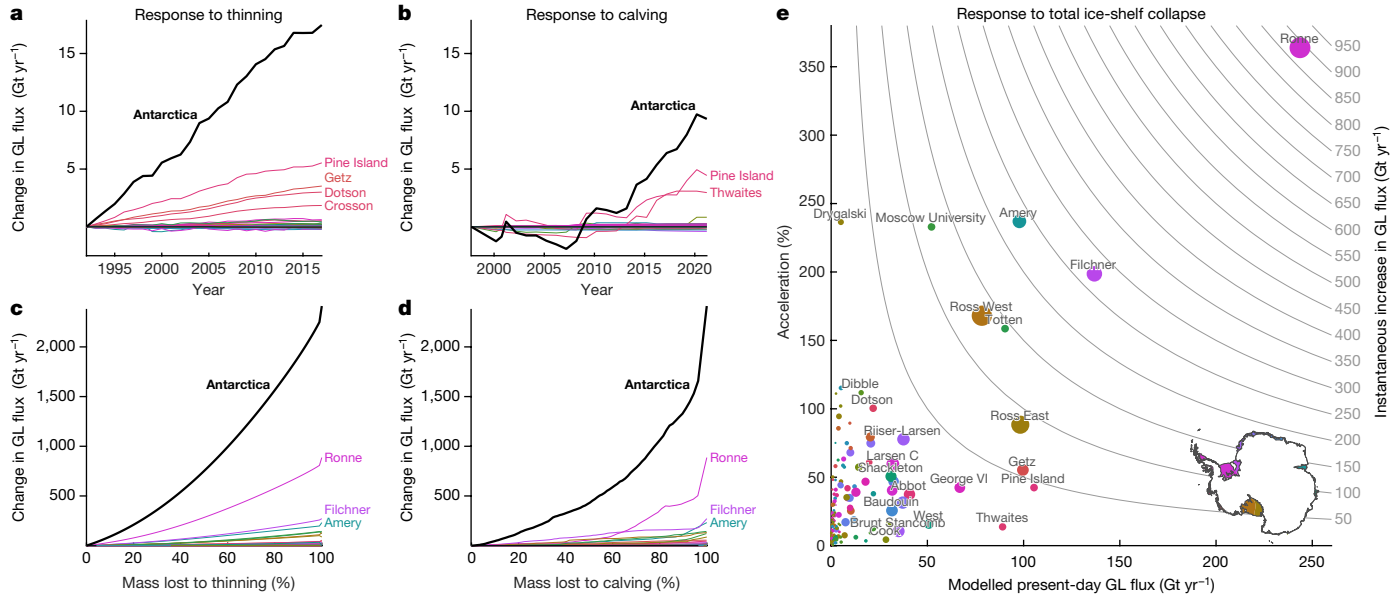


**Fig. 4 | Modelled instantaneous response to forcing. a**,**b**, Holding all other variables constant, we model the instantaneous grounding-line (GL)-flux response relative to a control run for annual observations of ice-shelf thickness (**a**) and calving-front locations (**b**) since the 1990s. Among all 181 ice shelves, Pine Island shows the greatest sensitivity to observed thinning and calving-front retreat. **c**,**d**, The instantaneous response to a range of ice-shelf thinning (**c**) and calving scenarios (**d**) (Supplementary Videos) suggests that total ice-shelf loss would most significantly impact the flow of the Ronne, Filchner and Amery ice shelves. **e**, The results for the case of 100% ice-shelf loss compare present-day ice flow to the hypothetical instantaneous response that would result from total ice-shelf collapse. In all panels, only select ice shelves are labelled, but data are shown nonetheless for all 181 ice shelves and grounded-ice termini, colour-scaled by central longitude. The area of the markers in **e** scales with ice-shelf area.

suddenly, with little warning, and can produce immediate increases in grounding-line flux and sea-level rise. Antarctic surface melt is expected to double by 2050[6], which significantly increases the likelihood of hydrofracture and the partial or wholesale ice-shelf collapse events, which skew sea-level projections significantly higher[8,47].

If the Antarctic Ice Sheet continues crumbling at its edges, marine ecosystems will be redefined, and a reorganized ocean circulation will impact primary productivity, water-mass formation and the delivery of heat to ice-shelf cavities[15–21]. We find that 5,874 ± 396 Gt of freshwater flux that has been injected into the Southern Ocean by the net loss of ice-shelf area over the past quarter of a century, superimposed on a background calving rate of 1,411 ± 28 Gt $yr^{-1}$, and the exclusion of net calving from ocean models has probably introduced large-scale systematic biases in sea-ice formation, ocean temperatures and salinities[20].

Since the major calving events from the Ross and Ronne ice shelves in the early 2000s, the overall extent of the Antarctic Ice Sheet has seen negligible regrowth (Fig. 2). Although most ice shelves have experienced a reduction in area over the past 20 years, pan-Antarctic totals of areal extents have been buoyed by gains from the largest ice shelves, which are all on track for major calving events sometime in the next decade (Fig. 3). Unless the Filchner, Ronne, Amery and Ross ice shelves all grow beyond their maximum observed extents, a continuation of their natural cycle could further reduce Antarctica's ice-shelf area by about 60,000 $km^2$ if their recent major calving events are repeated in the near future. Our modelling suggests that although none of the projected large calving events will have an appreciable impact on buttressing, continued reductions in ice-shelf area elsewhere around the continent could lead to an increase in sea-level contribution similar to that which has been driven by ice-shelf thinning in recent years.

## Online content

Any methods, additional references, Nature Research reporting summaries, source data, extended data, supplementary information, acknowledgements, peer review information; details of author contributions and competing interests; and statements of data and code availability are available at https://doi.org/10.1038/s41586-022-05037-w.


1. Fox-Kemper, B. et al. in *Climate Change 2021: The Physical Science Basis. Contribution of Working Group I to the Sixth Assessment Report of the Intergovernmental Panel on Climate Change*,Ch.9 (eds Masson-Delmotte, V. et al.) 1211–1362 (Cambridge Univ. Press, 2021).
2. Reese, R., Gudmundsson, G. H., Levermann, A. & Winkelmann, R. The far reach of ice-shelf thinning in Antarctica. *Nat. Clim. Change* **8**, 53–57 (2018).
3. Fürst, J. J. et al. The safety band of Antarctic ice shelves. *Nat. Clim. Change* **6**, 479–482 (2016).
4. Borstad, C. P. et al. A damage mechanics assessment of the Larsen B ice shelf prior to collapse: toward a physically-based calving law. *Geophys. Res. Lett.* **39**, L18502 (2012).
5. Scambos, T. A. et al. Ice shelf disintegration by plate bending and hydro-fracture: satellite observations and model results of the 2008 Wilkins ice shelf break-ups. *Earth Planet. Sci. Lett.* **280**, 51–60 (2009).
6. Trusel, L. D. et al. Divergent trajectories of Antarctic surface melt under two twenty-first-century climate scenarios. *Nat. Geosci.* **8**, 927–932 (2015).
7. Nowicki, S. et al. Experimental protocol for sea level projections from ISMIP6 stand-alone ice sheet models. *Cryosphere* **14**, 2331–2368 (2020).
8. Pattyn, F. et al. The Greenland and Antarctic ice sheets under 1.5 °C global warming. *Nat. Clim. Change* **8**, 1053–1061 (2018).
9. Seroussi, H. et al. ISMIP6 Antarctica: a multi-model ensemble of the Antarctic ice sheet evolution over the 21st century. *Cryosphere* **14**, 3033–3070 (2020).
10. DeConto, R. M. & Pollard, D. Contribution of Antarctica to past and future sea-level rise. *Nature* **531**, 591–597 (2016).
11. Edwards, T. L. et al. Revisiting Antarctic ice loss due to marine ice-cliff instability. *Nature* **566**, 58–64 (2019).
12. Bassis, J. N., Berg, B., Crawford, A. J. & Benn, D. I. Transition to marine ice cliff instability controlled by ice thickness gradients and velocity. *Science* **372**, 1342–1344 (2021).
13. Crawford, A. J. et al. Marine ice-cliff instability modeling shows mixed-mode ice-cliff failure and yields calving rate parameterization. *Nat. Commun.* **12**, 2701 (2021).
14. Clerc, F., Minchew, B. M. & Behn, M. D. Marine ice cliff instability mitigated by slow removal of ice shelves. *Geophys. Res. Lett.* **46.21**, 12108–12116 (2019).
15. Cape, M. R., Vernet, M., Kahru, M. & Spreen, G. Polynya dynamics drive primary production in the Larsen A and B embayments following ice shelf collapse. *J. Geophys. Res. Oceans* **119**, 572–594 (2014).
16. Campagne, P. et al. Glacial ice and atmospheric forcing on the Mertz Glacier Polynya over the past 250 years. *Nat. Commun.* **6**, 6642 (2015).
17. Clarke, A. et al. Climate change and the marine ecosystem of the western Antarctic Peninsula. *Phil. Trans. R. Soc. B* **362**, 149–166 (2007).
18. Grosfeld, K., Schröder, M., Fahrbach, E., Gerdes, R. & Mackensen, A. How iceberg calving and grounding change the circulation and hydrography in the Filchner Ice Shelf–Ocean System. *J. Geophys. Res. Oceans* **106**, 9039–9055 (2001).

19. Silva, T. A. M., Bigg, G. R. & Nicholls, K. W. Contribution of giant icebergs to the Southern Ocean freshwater flux. *J. Geophys. Res. Oceans* **111**, C03004 (2006).
20. Stern, A. A., Adcroft, A. & Sergienko, O. The effects of Antarctic iceberg calving-size distribution in a global climate model. *J. Geophys. Res. Oceans* **121**, 5773–5788 (2016).
21. Yoon, S.-T. et al. Ice front retreat reconfigures meltwater-driven gyres modulating ocean heat delivery to an Antarctic ice shelf. *Nat. Commun.* **13**, 306 (2022).
22. Gutt, J. et al. Biodiversity change after climate-induced ice-shelf collapse in the Antarctic. *Deep Sea Res. II* **58**, 74–83 (2011).
23. Adusumilli, S., Fricker, H. A., Medley, B., Padman, L. & Siegfried., M. R. Interannual variations in meltwater input to the Southern Ocean from Antarctic ice shelves. *Nat. Geosci.* **13**, 616–620 (2020).
24. Mohajerani, Y., Wood, M., Velicogna, I. & Rignot, E. Detection of glacier calving margins with convolutional neural networks: a case study. *Remote Sensing* **2019**, 74 (2019).
25. Miles, B. W. J., Stokes, C. R. & Jamieson, S. S. R. Pan–ice-sheet glacier terminus change in East Antarctica reveals sensitivity of Wilkes Land to sea-ice changes. *Sci. Adv.* **2**, e1501350 (2016).
26. Greene, C. A., Young, D. A., Gwyther, D. E., Galton-Fenzi, B. K. & Blankenship, D. D. Seasonal dynamics of Totten Ice Shelf controlled by sea ice buttressing. *Cryosphere* **12**, 2869–2882 (2018).
27. Baumhoer, C. A., Dietz, A. J., Kneisel, C., Paeth, H. & Kuenzer, C. Environmental drivers of circum-Antarctic glacier and ice shelf front retreat over the last two decades. *Cryosphere* **15**, 2357–2381 (2021).
28. Scambos, T. et al. Calving and ice-shelf break-up processes investigated by proxy: Antarctic tabular iceberg evolution during northward drift. *J. Glaciol.* **54**, 579–591 (2008).
29. Lazzara, M. A., Jezek, K. C., Scambos, T. A., MacAyeal, D. R. & Van der Veen, C. J. On the recent calving of icebergs from the Ross Ice Shelf. *Polar Geogr.* **23**, 201–212 (1999).
30. MacAyeal, D. R. et al. Tabular iceberg collisions within the coastal regime. *J. Glaciol.* **54**, 371–386 (2008).
31. Rignot, E., Jacobs, S., Mouginot, J. & Scheuchl, B. Ice-shelf melting around Antarctica. *Science* **341**, 266–270 (2013).
32. Depoorter, M. A. et al. Calving fluxes and basal melt rates of Antarctic ice shelves. *Nature* **502**, 89–92 (2013).
33. Liu, Y. et al. Ocean-driven thinning enhances iceberg calving and retreat of Antarctic ice shelves. *Proc. Natl Acad. Sci. USA* **112**, 3263–3268 (2015).
34. Qi, M. et al. A 15-year circum-Antarctic iceberg calving dataset derived from continuous satellite observations. *Earth Syst. Sci. Data* **13**, 4583–4601 (2021).
35. Ferrigno, J. G. & Gould, W. G. Substantial changes in the coastline of Antarctica revealed by satellite imagery. *Polar Rec.* **23**, 577–583 (1987).
36. Paolo, F., Gardner, A. S., Greene, C. A. & Schlegel, N. J. *MEaSUREs ITS_LIVE Antarctic Ice Shelf Height Change and Basal Melt Rates, Version 1* (2022); NASA https://doi.org/10.5067/SE3XH9RXQWAM
37. Larour, E., Seroussi, H., Morlighem, M. & Rignot, E. Continental scale, high order, high spatial resolution, ice sheet modeling using the Ice Sheet System Model (ISSM). *J. Geophys. Res. Earth Surf.* **117**, F01022 (2012).
38. Gudmundsson, G. H., Paolo, F. S., Adusumilli, S. & Fricker, H. A. Instantaneous Antarctic ice sheet mass loss driven by thinning ice shelves. *Geophys. Res. Lett.* **46**, 13903–13909 (2019).
39. Sun, S. et al. Antarctic ice sheet response to sudden and sustained ice-shelf collapse (ABUMIP). *J. Glaciol.* **66**, 891–904 (2020).
40. De Rydt, J., Reese, R., Paolo, F. S. & Gudmundsson, G. H. Drivers of Pine Island Glacier speed-up between 1996 and 2016. *Cryosphere* **15**, 113–132 (2021).
41. Joughin, I., Shapero, D., Smith, B., Dutrieux, P. & Barham, M. Ice-shelf retreat drives recent Pine Island Glacier speedup. *Sci. Adv.* **7**, eabg3080 (2021).
42. Schlegel, N.-J. et al. Exploration of Antarctic Ice Sheet 100-year contribution to sea level rise and associated model uncertainties using the ISSM framework. *Cryosphere* **12**, 3511–3534 (2018).
43. Robel, A. A. & Banwell, A. F. A speed limit on ice shelf collapse through hydrofracture. *Geophys. Res. Lett.* **46**, 12092–12100 (2019).
44. Goldberg, D. N., Heimbach, P., Joughin, I. & Smith, B. Committed retreat of Smith, Pope, and Kohler Glaciers over the next 30 years inferred by transient model calibration. *Cryosphere* **9**, 2429–2446 (2015).
45. Lilien, D. A., Joughin, I., Smith, B. & Gourmelen, N. Melt at grounding line controls observed and future retreat of Smith, Pope, and Kohler glaciers. *Cryosphere* **13**, 2817–2834 (2019).
46. Pattyn, F., Huyghe, A., De Brabander, S. & De Smedt, B. Role of transition zones in marine ice sheet dynamics. *J. Geophys. Res. Earth Surf.* **111**, eabg3080 (2006).
47. Edwards, T. L. et al. Projected land ice contributions to twenty-first-century sea level rise. *Nature* **593**, 74–82 (2021).
48. Massom, R. A. et al. External influences on the Mertz Glacier Tongue East Antarctica in the decade leading up to its calving in 2010. *J. Geophys. Res. Earth Surf.* **120**, 490–506 (2015).
49. Fricker, H. A., Young, N. W., Allison, I. & Coleman, R. Iceberg calving from the Amery ice shelf, East Antarctica. *Ann. Glaciol.* **34**, 241–246 (2002).
50. Walker, C. C., Becker, M. K. & Fricker, H. A. A high resolution, three-dimensional view of the D-28 calving event from Amery Ice Shelf with ICESat-2 and satellite imagery. *Geophys. Res. Lett.* **483**, e2020GL091200 (2021).

# Methods

### Extended thickness, velocity and mask grids

In developing the coastline and calving flux estimates described below, we needed gridded thickness and velocity datasets that fully cover the maximum known extents of the ice sheet, without any data gaps. Most publicly available datasets, however, contain data gaps or are masked to ice-sheet extents that correspond to a single snapshot in time. To create continuous grids that cover the full domain of interest, we combine multiple thickness and velocity datasets and extend them to cover the maximum observed ice-sheet extents as follows.

**Velocity.** Separately for the *x* and *y* velocity directions, we compute the error-weighted average of the ITS_LIVE version 1 mosaic[51] and MEaSUREs InSAR-Based Antarctica Ice Velocity Map, Version 2[52], then fill any remaining internal holes using the regionfill algorithm in MATLAB, which smoothly interpolates by computing a discrete Laplacian and solving the Dirichlet boundary value problem. Flow directions are extrapolated beyond observed extents of the ice sheet by multiplying observed velocities by the observed thickness mosaic (described below), then an inpainting algorithm is used to fill the entire domain. Velocity magnitudes (speeds) are then propagated constantly along the hypothetical direction of flow. We multiply velocity by thickness before inpainting, rather than inpainting velocities $v$–$x$ and $v$–$y$ directly, to give appropriate weight to flow directions of thicker ice that carries more flux. The rationale for constant extrapolation is to make the simplest possible assumption about ice dynamics beyond the observed extents of the ice sheet, and significant deviations from the constant assumption are unlikely, given that velocities are rarely extrapolated by distances greater than a few kilometres. The resulting complete velocity grid is shown in Extended Data Fig. 3. We note that the extrapolated velocity data in Extended Data Fig. 3 may appear somewhat fantastical as the Southern Ocean is filled with unrealistic streaks of ice flow, but we reiterate that we only use data from within the maximum known extents of the ice sheets, where our extrapolations are realistic and proximal to direct observations.

**Thickness.** The ice-thickness grid we use is primarily based on BedMachine Antarctica Version 2[53]. BedMachine contains zero ice thickness in some locations that are known to have been part of the ice sheet during some portion of our study period. For example, most of Larsen B and half of the Mertz Glacier Tongue broke away before BedMachine was created. Elsewhere, some ice-shelf edges were clipped away owing to masking in the creation of the BedMachine dataset. Therefore, in any tidal regions where BedMachine contains zero ice thickness, we fill grid cells with the most-recent-available thickness data obtained through a hydrostatic assumption applied to surface elevations starting with the Reference Elevation Map of Antarctica (REMA)[54], then Bedmap2[55], then the Antarctic 1-km digital elevation model from Combined ERS-1 Radar and ICESat Laser Satellite Altimetry, Version 1[56], then Radarsat Antarctic Mapping Project (RAMP2)[57]. The BedMachine thickness field natively has firn air content removed; therefore, to convert surface elevations from other datasets to an equivalent ice thickness, we reference surface elevations to the geoid as needed, subtract the mean firn air content from the Glacier Energy and Mass Balance (GEMB) module in ISSM, then invert for thickness assuming that the density of ice is 917 kg $m^{-3}$ and the density of seawater is 1,027 kg $m^{-3}$. After building a mosaic from the aforementioned thickness and surface-elevation datasets, we then extrapolate constant thickness in the direction of flow, following the same technique we used for constant extrapolation of velocities. The resulting complete thickness grid is shown in Extended Data Fig. 3.

**Ice-shelf masks.** To quantify changes in the area and mass of each ice shelf, we create a gridded mask of 181 ice-shelf names based on the MEaSUREs Antarctic Boundaries for IPY 2007–2009 from Satellite Radar, Version 2[58]. We dilate the boundaries of each ice shelf by 100 km in all directions, then use constant extrapolation along flowlines following the procedure described above for velocity and thickness. The result shown in Extended Data Fig. 3 is a set of masks that cover areas much larger than any observed ice-shelf extents, but are certain to fully capture changes at the ice front while providing extra tolerance in the grounding zone, which is beneficial when working with multiple datasets that may have been created with different grounding-line masks. The ice-shelf mask in Extended Data Fig. 3 shows the fully dilated ice-shelf areas; although, to be clear, we limit analysis of the area and mass of each ice shelf to pixels where ice is observed and the BedMachine mask indicates ice shelf or ocean.

### Coastline time series

To generate 24 roughly annual coastlines from 1997 to 2021, we combined manual coastline picks from the following four data sources.

**RAMP.** We used the Radarsat Antarctic Mapping Project (RAMP) Antarctic Mapping Mission-1 coastline in the after_coast_continuous.shp file for late 1997[59] and the RAMP Modified Antarctic Mapping Mission cst2000line.shp, which corresponds to late 2000.

**MOA.** We use coastlines provided by the MODIS Mosaic of Antarctica (MOA) project for the years 2004, 2009 and 2014[60].

**MODIS.** For annual coastlines from March 2000 to March 2017, we interpolate ice-sheet areas in a 1-km-resolution optical- and thermal-band Moderate Resolution Imaging Spectroradiometer (MODIS)-based fast-ice dataset[61] to our 240-m-resolution grid. The same procedure was also applied to the same type of MODIS data for March 2021.

**Sentinel 1a.** For each year from March 2015 to March 2021, we digitize coastlines using the same methods that were used to generate the annual MODIS-based fast-ice dataset, but we apply the methods to Sentinel 1a radar image mosaics from http://seaice.dk/ that were collected concurrently with the MODIS data each March, thus providing two independent datasets obtained from different types of sensor.

**Combining datasets.** All coastlines were masked to the 240-m-resolution ITS_LIVE Antarctic mosaic grid. We immediately found that the uncorrected masks from each dataset are not directly intercomparable, as different research groups sometimes differ in how they designate ice types, different sensors vary in their ability to differentiate shelf ice from sea ice, and certain islands are included in some coastline datasets but neglected in others. To ensure that any changes we see from one coastline mapping to the next reflect true changes in coastline rather than changes in sensors or methodology, we create a composite dataset by adjusting each contributing dataset as follows. After each adjustment described in the following, any potential new holes in any ice mask are filled to preserve a continuous ice sheet. (1) Remove the attached iceberg D15 from all datasets, because D15 calved from West Ice Shelf in 1992, then abutted the coast for decades after[62] and appears in some coastline products but not others. (2) Remove any islands that are not present in all datasets. (3) Remove from the MODIS-based data any ice that is present in all 18 MODIS-based mappings but does not appear in any other datasets. Add to all MODIS-based data any ice that is present in all other datasets but does not appear in any of the MODIS-based data. (4) Remove from the Sentinel 1a-based data any ice that is present in all seven years of Sentinel 1a mappings but does not appear in any other datasets. Add to all Sentinel 1a data any ice that is present in all other datasets but does not appear in any of the Sentinel 1a data. (5) Remove from the MOA-based data any ice that is present in all three MOA-based mappings but does not appear in any other datasets. Add to all MOA data any ice that is present in all other datasets but does not appear in any of the MOA-based data.

(6) Add to all RAMP-based data any ice that is not present in either of the RAMP mappings but is present in all other datasets. (7) Using the years 2015, 2016, 2017 and 2021 when the same techniques were applied to MODIS and Sentinel 1a data collected concurrently, we remove from both datasets any ice that does not appear at least once in each dataset. (8) Add to all datasets any ice that is present within all three MOA coastlines, but is not present in any of the three concurrent MODIS-based mappings. (9) Use projected $x$ and $y$ velocity components $v_x$ and $v_y$ to calculate grid-cell centre displacements that should occur, in increments of six months, up to six years for the entire grid. For this step we multiply $v_x$ and $v_y$ by 1.1, which allows some tolerance for variations in velocity, which we describe below. (10) It is evident by inspection that the 1997 RAMP coastline was digitized at higher resolution and with greater care than the 2000 RAMP coastline. Therefore, we put some faith in the 1997 coastline as a more reliable reference. Using the expected displacements from the velocity fields to tell us the maximum amount of coastline growth that could possibly occur from 1997 to 2000, including the 10% velocity tolerance, any ice that is present in the 2000 mask but is missing from the 1997 mask, and could not have advected to the new location in just three years, is removed from the 2000 mask. (11) Adjust the MOA2004 mask following the same logic described in the previous step, but tie MOA2004 to RAMP2000 and MOA2009. Any pixels in MOA2004 that could have advected from ice that is present in RAMP2000 and will advect to a location that will appear as ice in MOA2009, then must be ice in MOA2004. Similarly, any ice that is present in MOA2004, but could not have advected there from RAMP2000 and will not advect to an ice location in MOA2009, cannot be ice in MOA2004. Adjust MOA2004 accordingly. (12) Follow the previous step to tie MOA2009 to the adjusted MOA2004 and MOA2014. (13) Tie MOA2014 to MOA2009 and any ice that is present in both the Sentinel 1a- and MODIS-based mappings for 2021. (14) The adjusted RAMP, MOA and combined 2021 mappings now serve as anchors to tie the MODIS- and Sentinel 1a-based mappings. Following the same method described above, tie each annual MODIS- and Sentinel 1a-based mapping to the closest past and future anchor mappings.

The resulting 24 ice masks achieve higher resolution than the underlying MODIS or Sentinel 1a mosaics because we exploit the offset of the MODIS and Sentinel 1a mosaic grids, and because we use known velocity to interpolate coastline migration between coarse-resolution grid postings to create our 240-m grid.

We note that some islands do not appear in every constituent dataset, so through the methods described above, we have constrained them to a constant area, or a nearly constant area in some cases where the algorithm introduces or otherwise allows a small amount of noise. As a result, if any bias exists in our overall estimates of ice-sheet-area change, we suspect it would be towards underestimation of area reduction, because most islands are small, susceptible to changes in their environment and located around the Antarctic Peninsula, where major reductions in ice-shelf area are known to have occurred.

We have the most confidence in our ice-shelf-area time series that show the largest amplitudes of change, so we recommend considering the range of values that are presented in Supplementary Information and Supplementary Table 1 when interpreting the time series of smaller ice shelves or ice shelves that are adjacent to any islands that may not appear in all contributing datasets.

### Ice-shelf-area and -mass time series calculation

Ice-shelf-area time series shown in Fig. 2 and Supplementary Information were created by summing the areas of all ice grid cells that are classified as ocean or ice shelf in the BedMachine mask. Grid-cell areas are corrected for polar stereographic distortion using the psdistortion function in Antarctic Mapping Tools for MATLAB, and sums are calculated for each of the 181 ice shelves in the dilated ice-shelf mask. Any ice outside the 181 dilated ice-shelf masks is collectively summed as 'other' in Supplementary Table 1. Ice-shelf-mass time series are calculated by the same summing method as the ice-shelf-area time series, where the mass of each grid cell is calculated as its area multiplied by thickness and the density of ice, 917 kg $m^{-3}$.

**Error estimation.** Uncertainty in the ice-shelf-area time series stems from error in the location of the coastline, which we estimate as ±1 pixel across the entire front of each ice shelf. We assume coastline-picking errors are fully correlated for each ice shelf, and we therefore estimate the area error for each ice shelf as the sum of the area of all of the ice shelf's grid cells that are directly adjacent to the ocean. To estimate the total area error for the entire continent, we assume area errors are independent between ice shelves, and therefore take the root sum square of all 181 ice-shelf errors and all areas classified as other. Errors in the ice-shelf-mass time series are calculated as the root sum square of errors related to area uncertainty and errors related to thickness uncertainty. Mass errors caused by area uncertainty are calculated by summing the mass of all ocean-adjacent grid cells for each ice shelf. Mass errors caused by thickness uncertainty are calculated by adding 30 m of thickness to all grid cells that experience any change between ice and ocean at any time throughout the observation period. We estimate that 30 m is more than sufficient to account for errors in firn air content and errors in the surface-elevation measurements that were used to calculate ice-shelf thickness. Within each ice shelf, we assume thickness errors are fully correlated, and we therefore sum all thickness-related uncertainties for each ice shelf. We calculate the total mass uncertainty of each ice shelf as the root sum square of thickness- and area-related errors, and we calculate pan-Antarctic total mass uncertainty as the root sum square of all 181 ice-shelf and other mass uncertainties. We note that the mean pan-Antarctic area uncertainty estimate (1,465 $km^2$) is cut in half (771 $km^2$) when areas that do not terminate in ice shelves are excluded, whereas the mean mass uncertainty of 396 Gt drops only to 378 Gt in this case owing to the relatively thin ice found in coastal areas that do not terminate in ice shelves.

**Additional 'calveats'.** The outline of Thwaites Glacier's ice shelf is notoriously difficult to delineate, regardless of the sensor that is used. A number of laudable efforts have been made to track evolving extents of Thwaites at high resolution[63–65] but despite the sound methods that have been used by each study we are aware of, the resulting coastlines often disagree by tens of kilometres. The manually delineated coastlines on which our composite product is based contain many of the same types of disagreement, and although we have constrained our coastlines to ensure that the rate of ice-front advance never exceeds realistic velocities, in some years our coastline takes the shape of an implausible compromise between the various input datasets. The mass time series for Thwaites also relies on a particularly far extrapolation from the nearest thickness measurement. Accordingly, the exact timing and magnitude of mass changes presented for Thwaites Glacier should be interpreted loosely, but we note that the overall changes that have occurred between 1997 and 2021 are nonetheless well constrained. At Thwaites Glacier and elsewhere, we encourage close inspection of the agreement between our composite coastline and the constituent data in time series in Supplementary Information. We also recommend comparing our coastline product to available satellite imagery where it is possible.

Some ice shelves are known to have retreated significantly before the acquisition date of the input velocity and thickness data we use in our study. Our technique handles these cases well over short distances, but in the case of Larsen B and Scar Inlet, we use thickness data derived from RAMP whereas we extrapolate velocities from the present-day coastlines (Extended Data Fig. 3).

**Iceberg A76.** In May 2021, just two months after our final annual MODIS and Sentinel 1a-based mappings, Iceberg A76 calved from the western side of Ronne Ice Shelf. Although we do not capture the A76 event

in any of our 24 pan-Antarctic coastline mappings, we can estimate from previous area and mass changes that the reported 4,320-km$^2$ tabular berg (https://www.esa.int/ESA_Multimedia/Images/2021/05/Meet_the_world_s_largest_iceberg) equates to about 1,002 Gt of ice loss from the Ronne Ice Shelf (Extended Data Fig. 4).

### Steady-state mass flux

In addition to interannual mass variability owing to changes in coastal extents, we also calculate steady-state mass flux across the calving front and grounding line of each ice shelf. Mass-flux calculations are performed directly on the gridded velocity and thickness data as follows. (1) For the steady-state calving flux calculation, we define a gridded mask that is true wherever grid cells are ice throughout the entirety of our observation period, representing the minimum observed extents of the ice sheet. For steady-state grounding-line-flux calculations, we define a gridded mask that is true for all grid cells that are identified as grounded or rock in the BedMachine mask. (2) Pixel centre locations $(x_0, y_0)$ of the 240-m resolution ITS_LIVE grid are advected to the predicted locations $(x_1, y_1)$ after one year of ice flow (Extended Data Fig. 5). To allow for any acceleration or curvature that may occur during the year of advection, we use ten steps of one-tenth of a year displacements between $(x_0, y_0)$ and $(x_1, y_1)$. (3) For both calving-flux and grounding-line-flux calculations, we bilinearly interpolate the respective mask at locations $(x_1, y_1)$, which gives the fraction of each grid cell that is ice or grounded after one year of advection (Extended Data Fig. 5). (4) The annual mass flux across the mask boundary is calculated by multiplying the mass of each grid cell by the fraction of the grid cell that crosses into the false region of the mask during the year of advection.

**Error estimation.** Steady-state mass-flux error can result from thickness error or velocity error. To quantify the effects of thickness error, we use BedMachine's bed elevation error estimates as the thickness error estimate for grounded ice, and we assume 30-m-thickness error for floating ice. We add the estimated thickness error to our thickness measurement and recalculate the steady-state grounding-line flux and calving flux. For each ice shelf, we assume the difference between the two flux calculations represents the error owing to thickness error. Similarly, where velocity error estimates are available, we add estimated velocity errors to $v_x$ and $v_y$ in the direction of flow, recalculate pixel centre locations $(x_1, y_1)$ using the increased velocities and recalculate the mass flux out of the mask. Velocity-induced errors are taken as the difference between the two calculations. For each ice shelf, we take the mass-flux error as the root sum square of thickness- and velocity-induced flux errors, and for the pan-Antarctic total error estimate we take the root sum square of all 181 ice shelves along with the regions classified as other.

We note that our gridded velocity field is an error-weighted mosaic of many millions of satellite images acquired as early as 1985, but the data are weighted heavily towards recent years, because most of the high-quality data have been collected since the 2013 launch of Landsat 8. Meanwhile, thickness data for ice shelves is largely from the REMA mosaic, which was compiled from data collected over a much shorter timespan. The long duration over which the velocity measurements were acquired, together with the snapshot of ice-shelf thickness we use, result in flux estimates that neither correspond to a clearly defined date nor provide a representative long-term average. Accordingly, at any given time, the true mass-flux rate could deviate from the nominal value beyond our estimated errors owing to fluctuations in ice velocity or thickness.

### Ice-shelf thickness change

Ice-shelf mass change owing to ice-shelf thinning or thickening since 1997 is taken from a 3-km-resolution, quarterly, gridded ice-shelf-thickness data product[36]. Linear trends in thickness are calculated for each grid cell from December 1997 to the end of the altimetry record in December 2017. We calculate the area of each grid cell, including a correction for polar stereographic distortion, and multiply area by thickness trend and ice density to obtain a mass rate in units of Gt yr$^{-1}$ for each grid cell. To create Extended Data Fig. 2, for each ice shelf, mass rates of all of its grid cells are summed and multiplied by 23.5 to obtain an estimate of total ice-shelf-mass change from late 1997 to early 2021. When summing mass rates for each ice shelf, we only consider grid cells that were observed to be ice in every coastline mapping from 1997 to 2017.

**Error estimation.** We use formal error estimates taken from the residuals of the ice-shelf-thickness data. For each grid cell, we propagate formal uncertainties for the thickness trend (equation 8.17 on page 188 in ref. [66]), then for each ice shelf we sum the error estimates of all grid cells, which assumes errors are fully correlated within each ice shelf. For Antarctica's total ice-shelf-mass-rate error estimate, we assume errors are independent between ice shelves, and we take the root sum square of estimated errors for all 181 ice shelves and any grid cells that are classified as other in our mask.

### Surface mass balance

Although we do not directly report on surface processes in this paper, we include surface-mass-balance estimates in Supplementary Table 1 as they may provide context for the observed thickness changes. Following a method similar to that described above for thickness change, we sum the surface-mass-balance trends of all grid cells within each ice shelf to obtain the total surface mass balance for each ice shelf. The pan-Antarctic total surface-mass-balance trend is taken as the root sum square of all 181 ice shelves and any grid cells classified as other in our mask.

### Ice-sheet model

**Model set-up.** Our ice-sheet model experiments rely on the ISSM framework[37]. The model domain covers the Antarctic Ice Sheet at its cumulative maximum extent from 1997 to 2021. That is, any grid cell that was observed to contain ice during that period was included in the model domain. The initial model geometry is from BedMachine Antarctica Version 2[53]. To maintain numerical consistency between all experiments, we use the same high-resolution model mesh initialized as follows. The model resolution ranges from 100 m in areas with the largest gradients in surface elevation and ice velocity, to 75 km in the Antarctic high interior. In addition, all floating ice has a resolution of 5 km or finer, and within regions where the ice-mask changes state between ice and no-ice over our observational period, the spatial resolution is 100 m or finer. This set-up results in a total of 20,746,993 mesh elements.

Model initialization follows that described by ref. [42] with adaptions outlined in by ref. [9] for JPL_ISSM, including a step for data assimilation[67] of the present-day geometry conditions and ice surface velocities[51] derived by this study on an extended mask (see 'Extended thickness, velocity and mask grids'). The assimilation step serves to infer the unknown basal friction coefficient for all grounded ice and the ice viscosity for all floating ice. For ice viscosity over grounded ice, we take advantage of ice viscosity calculated on a lower-resolution mesh by ref. [42], using a mesh initialized with a geometry from BedMachine v2, extruded to 15 layers, distributed such that they increase by 10% with increased height. Ice temperature was solved assuming an ice thermal steady state[68], using a higher-order[69,70] approximation for stress balance and then used to calculate an effective two-dimensional ice viscosity using the depth-averaged ice temperature. Here we bilinearly interpolate their ice viscosity field onto our mesh domain.

Once ice viscosity and the basal friction coefficient fields are defined on our high-resolution mesh, we run the model forwards for one year, holding the grounding-line location constant, but allowing the ice geometry to relax in response to the initial model configuration, forcing

and boundary conditions, which are not temporally consistent datasets. This procedure is a particularly critical step for modelling the areas of the domain that are extended beyond that of the present-day ice sheet, and are, in most cases, extrapolated outwards from current observations (see 'Extended thickness, velocity and mask grids'). This procedure ensures that the model geometry is consistent with modelled ice velocities before conducting any perturbation sensitivity experiments. The resulting model state, after relaxation, defines the initial conditions for all ISSM stress-balance experiments.

With the exception of the calculation of thermal steady state described above, all model-initialization and stress-balance calculations use the two-dimensional Shelfy–Stream approximation[71]. The Shelfy–Stream approximation considers longitudinal stresses, so it is a highly appropriate stress-balance approximation for the regions of interest here, including ice shelves and fast-flowing regions with low driving stresses. To ensure that our stress-balance calculation equation converges without spurious results, so that model sensitivity can be determined through comparison against a control simulation, we set a stress-balance relative tolerance of $10^{-5}$. The friction law, used by default in ISSM, is linear viscous, as described by ref. [37].

**Model experiments.** Each model experiment consists of a suite of model calculations of an instantaneous stress-balance response to a perturbation in either the calving front or to the thickness of floating ice. We also conduct a control simulation by running a stress-balance calculation on the model geometry resulting from the initialization and relaxation methods described above. For the calving-front-change simulations, we alter the calving front by changing the model ice mask. For the thickness-change simulations, we alter the ice thickness of the floating ice by changing the model geometry (ice thickness, ice surface and ice base), such that the new thickness is in hydrostatic equilibrium with the ocean water. Once the ice-sheet geometry or extent is altered, we solve a stress-balance calculation, resulting in an estimate of a two-dimensional velocity field over the entire model ice domain. Historical calving experiments are conducted for 1997 to 2021, which corresponds to our calving-front observations, and historical ice-shelf thinning experiments are conducted for 1992 to 2017, when pan-Antarctic ice-shelf thickness observations are available.

**Model comparison.** An ice-sheet model can never be fully validated until nature sweeps through a range of test scenarios and complete observations come available to measure the ice-sheet response. Until then, we can only use the observations that are available to tune and evaluate the performance of our model, and we can compare against other models that have been accepted by the community. In this work, we tune the model to match velocity observations, we compare the modelled grounding-line flux to the observed grounding-line flux, and we perform a model run to compare directly with published results from a previous modelling study that uses a very similar set-up to ours. Extended Data Fig. 6 shows modelled values of the grounding-line flux of individual ice shelves for the ISSM control run. Overall, modelled mean values are biased high (2,163 Gt $yr^{-1}$) in the control run relative to observations (1,899 Gt $yr^{-1}$). Accordingly, we use the model only to test sensitivities to perturbations relative to the control. Extended Data Fig. 7 shows one such sensitivity experiment, in which we recreate the results of a previous paper that used a different ice-sheet model[38].

**Instantaneous response.** To quantify the effects of changing ice-shelf geometry, we consider the instantaneous velocity response to each change, relative to a control run. Using a stress-balance approach, we test thinning and calving independently, but their combined effects on buttressing may be approximated by a linear combination of the independent experiments when perturbations are small.

We found that in a few nodes corresponding to small, grounded ice rumples or ice rises, total loss of the surrounding ice shelf produced unrealistically high-velocity responses. To address the issue, the velocity of any node that suddenly exceeds 10,000 m $yr^{-1}$ was set to its last velocity in the experiment before it exceeded the velocity threshold. We note that the issue of instability is rare, however, and our need to govern velocities never affected more than 407 of 10,529,015 nodes in any particular run. We note that the 10,000 m $yr^{-1}$ velocity threshold was applied in the analysis after the model was run, and it is not part of ISSM.

**Grounding-line flux.** In the instantaneous response, grounded ice thickness change is neglected, because by nature, we only solve for a stress balance without consideration to mass transport; therefore, the ice does not transiently draw down. Thus, grounding-line-flux anomalies are calculated purely from the modelled magnitude of the velocity response. We discard nodes directly adjacent to ice shelves, then use natural-neighbour interpolation to obtain velocity magnitudes along the BedMachine grounding line from the irregularly spaced grounded ISSM nodes. Velocity magnitudes are multiplied by flow unit vectors, and the flux through the gate is calculated following the method described in ref. [72] as

$$\text{Flux} = \sum (\mathrm{d}x v_y - \mathrm{d}y v_x) H \rho_{\text{ice}},$$

where d$x$ and d$y$ are the $x$ and $y$ spacing (gradient) along the grounding line, $H$ is the ice thickness along the grounding line and $\rho_{\text{ice}} = 917$ kg $m^{-3}$ is the ice density. By calculating the grounding-line flux in this way, we are able to easily obtain flux values within each dilated ice-shelf mask that we use for analysis of the observed thinning and calving data. Flux values are summed individually for each of the 181 ice shelves and all areas identified as other.

## Data availability

We use velocity data from ITS_LIVE[51], which is available at https://its-live.jpl.nasa.gov/ and MEaSUREs InSAR-Based Antarctica Ice Velocity Map, Version 2[52], which is available at https://doi.org/10.5067/D7GK8F5J8M8R. Static ice-thickness data are primarily from BedMachine Antarctica Version 2[53], which is available at https://doi.org/10.5067/E1QL9HFQ7A8M. We also use surface elevation data from REMA[54] (https://www.pgc.umn.edu/data/rema/), Bedmap2[55] (https://www.bas.ac.uk/project/bedmap-2/), Antarctic 1-km digital elevation model from Combined ERS-1 Radar and ICESat Laser Satellite Altimetry, Version 1[56] (https://doi.org/10.5067/H0FQ1KL9NEKM) and Radarsat Antarctic Mapping Project Digital Elevation Model, Version 2[57] (https://doi.org/10.5067/8JKNEW6BFRVD). Ice-shelf masks are adapted from MEaSUREs Antarctic Boundaries for IPY 2007–2009 from Satellite Radar, Version 2[58] (https://doi.org/10.5067/AXE4121732AD). Ice-shelf-thickness time series[36] are available at http://its-live-data.s3.amazonaws.com/height_change/Antarctica/Floating/ANT_G1920V01_IceShelfMelt.nc. Radarsat-derived coastlines[59] are available at https://asf.alaska.edu/data-sets/derived-data-sets/ramp/ramp-get-ramp-data/, coastlines from MODIS Mosaic of Antarctica[60] are available at https://doi.org/10.5067/68TBT0CGJSOJ and coastlines from the fast-ice dataset[61] are available at https://doi.org/10.26179/5d267d1ceb60c. Sentinel 1b-based mosaics used in this work are available at http://seaice.dk/. Our final, processed ice-shelf-thickness and -mass time series data are presented in Supplementary Table 1 and are also available in .mat format at https://github.com/chadagreene/ice-shelf-geometry. The coastline data presented in this work are available as plain-text files of ice-sheet outlines and also as binary grids at 240-m resolution in .mat format at https://doi.org/10.5281/zenodo.5903643.

## Code availability

Analysis and figure generation were performed in MATLAB, with functions from Antarctic Mapping Tools for MATLAB[73] and the Climate

Data Toolbox for MATLAB[74]. All code that was developed for this work to generate coastlines, analyse the data and produce the figures is available at https://github.com/chadagreene/ice-shelf-geometry. Ice-shelf surface elevation time series were processed with the Cryosphere Altimetry Processing Toolkit, which is available at https://doi.org/10.5281/zenodo.3665785. The ISSM and GEMB models used in this work are open-source and publicly available at https://issm.jpl.nasa.gov.


51. Gardner, A. S., Fahnestock, M. A. & Scambos, T. A. *ITS_LIVE Regional Glacier and Ice Sheet Surface Velocities* (National Snow and Ice Data Center, 2019); https://doi.org/10.5067/6II6VW8LLWJ7
52. Rignot, E., Mouginot, J. & Scheuchl, B. *MEaSUREs InSAR-Based Antarctica Ice Velocity Map, Version 2* (NASA National Snow and Ice Data Center Distributed Active Archive Center, 2017); https://doi.org/10.5067/D7GK8F5J8M8R
53. Morlighem, M. *MEaSUREs BedMachine Antarctica, Version 2* (NASA National Snow and Ice Data Center Distributed Active Archive Center, 2020); https://doi.org/10.5067/E1QL9HFQ7A8M
54. Howat, I. M., Porter, C., Smith, B. E., Noh, M. J. & Morin, P. The reference elevation model of Antarctica. *Cryosphere* **13**, 665–674 (2019).
55. Fretwell, P. et al. Bedmap2: improved ice bed, surface and thickness datasets for Antarctica. *Cryosphere* **7**, 375–393 (2013).
56. Bamber, J., Gomez-Dans, J. L. & Griggs, J. A. *Antarctic 1 km Digital Elevation Model (DEM) from Combined ERS-1 Radar and ICESat Laser Satellite Altimetry, Version 1* (NASA National Snow and Ice Data Center Distributed Active Archive Center, 2009); https://doi.org/10.5067/H0FQ1KL9NEKM
57. Liu, H., Jezek, K. C., Li, B. & Zhao, Z. *Radarsat Antarctic Mapping Project Digital Elevation Model, Version 2* (NASA National Snow and Ice Data Center Distributed Active Archive Center, 2015); https://doi.org/10.5067/8JKNEW6BFRVD
58. Mouginot, J., Scheuchl, B. & Rignot, E. *MEaSUREs Antarctic Boundaries for IPY 2007–2009 from Satellite Radar, Version 2* (NASA National Snow and Ice Data Center Distributed Active Archive Center, 2017; https://doi.org/10.5067/AXE4121732AD
59. Liu, H. & Jezek, K. A complete high-resolution coastline of Antarctica extracted from orthorectified radarsat SAR imagery. *Photogramm. Eng. Remote Sensing* **70**, 605–616 (2004).
60. Haran, T., Bohlander, J., Scambos, T., Painter, T. & Fahnestock, M. *MODIS Mosaic of Antarctica Image Map, Version 1* (NASA National Snow and Ice Data Center Distributed Active Archive Center, 2019); https://doi.org/10.5067/68TBT0CGJSOJ
61. Fraser, A. D. et al. High-resolution mapping of circum-Antarctic landfast sea ice distribution, 2000–2018. *Earth Syst. Sci. Data* **12**, 2987–2999 (2020).
62. Walker, C. C. et al. Iceberg, right ahead!: The surprising and ongoing collapse of an East Antarctic ice shelf in response to changes in the ocean environment. In *AGU Fall Meeting Abstracts* abstr. C13A-06 (AGU, 2019).
63. MacGregor, J. A., Catania, G. A., Markowski, M. S. & Andrews., A. G. Widespread rifting and retreat of ice-shelf margins in the eastern Amundsen Sea Embayment between 1972 and 2011. *J. Glaciol.* **58**, 458–466 (2012).
64. Miles, B. W. J. et al. Intermittent structural weakening and acceleration of the Thwaites Glacier Tongue between 2000 and 2018. *J. Glaciol.* **66**, 485–495 (2020).
65. Lhermitte, S. et al. Damage accelerates ice shelf instability and mass loss in Amundsen Sea Embayment. *Proc. Natl Acad. Sci. USA* **117**, 24735–24741 (2020).
66. Taylor, J. *Introduction to Error Analysis, the Study of Uncertainties in Physical Measurements* 2nd edn (University Science Books, 1997).
67. Morlighem, M. E. et al. Spatial patterns of basal drag inferred using control methods from a full-Stokes and simpler models for Pine Island Glacier, West Antarctica. *Geophys. Res. Lett.* **37**, L14502 (2010).
68. Seroussi, H. et al. Dependence of Greenland Ice Sheet projections on its thermal regime. *J. Glaciol.* **59**, 1024–1034 (2013).
69. Blatter, H. Velocity and stress-fields in grounded glaciers: a simple algorithm for including deviatoric stress gradients. *J. Glaciol.* **41**, 333–344 (1995).
70. Pattyn, F. A new three-dimensional higher-order thermomechanical ice sheet model: basic sensitivity, ice stream development, and ice flow across subglacial lakes. *J. Geophys. Res.* **108**, 2382 (2003).
71. MacAyeal, D. R. Large-scale ice flow over a viscous basal sediment. Theory and application to Ice Stream B, Antarctica. *J. Geophys. Res.* **94**, 4071–4087 (1989).
72. Gardner, A. S. et al. Increased West Antarctic and unchanged East Antarctic ice discharge over the last 7 years. *Cryosphere* **12**, 521–547 (2018).
73. Greene, C. A., Gwyther, D. E. & Blankenship, D. D. Antarctic mapping tools for MATLAB. *Comput. Geosci.* **104**, 151–157 (2017).
74. Greene, C. A. et al. The Climate Data Toolbox for MATLAB. *Geochem. Geophys. Geosyst.* **20**, 3774–3781 (2019).



**Acknowledgements** We thank ESA/Copernicus and R. Saldo of DTU Space/Technical University of Denmark for making Sentinel 1 mosaics available via http://seaice.dk. This research was supported by the NASA Postdoctoral Program, along with the NASA Cryospheric Science, Sea Level Change Team, and Modeling, Analysis and Prediction (MAP) Programs, and was conducted at the Jet Propulsion Laboratory, California Institute of Technology, under contract with the National Aeronautics and Space Administration ©2022 All rights reserved. This project received grant funding from the Australian Government as part of the Antarctic Science Collaboration Initiative program. We gratefully acknowledge computational resources and support from the NASA Advanced Supercomputing Division.


**Author contributions** C.A.G. and A.S.G. conceived of the study. A.D.F. compiled satellite imagery into mosaics and performed coastline delineation. C.A.G. wrote the code to generate velocity-constrained composite coastlines from multiple sources. N.-J.S. performed modelling experiments. C.A.G. analysed all observational and model data, generated all figures and wrote the first draft of the manuscript. All authors contributed to writing and revising the final manuscript.

**Competing interests** The authors declare no competing interests.

**Additional information**


**Supplementary information** The online version contains supplementary material available at https://doi.org/10.1038/s41586-022-05037-w.



**Correspondence and requests for materials** should be addressed to Chad A. Greene.



**Peer review information** *Nature* thanks Bertie Miles, Kiya Riverman and the other, anonymous, reviewer(s) for their contribution to the peer review of this work. Peer reviewer reports are available.

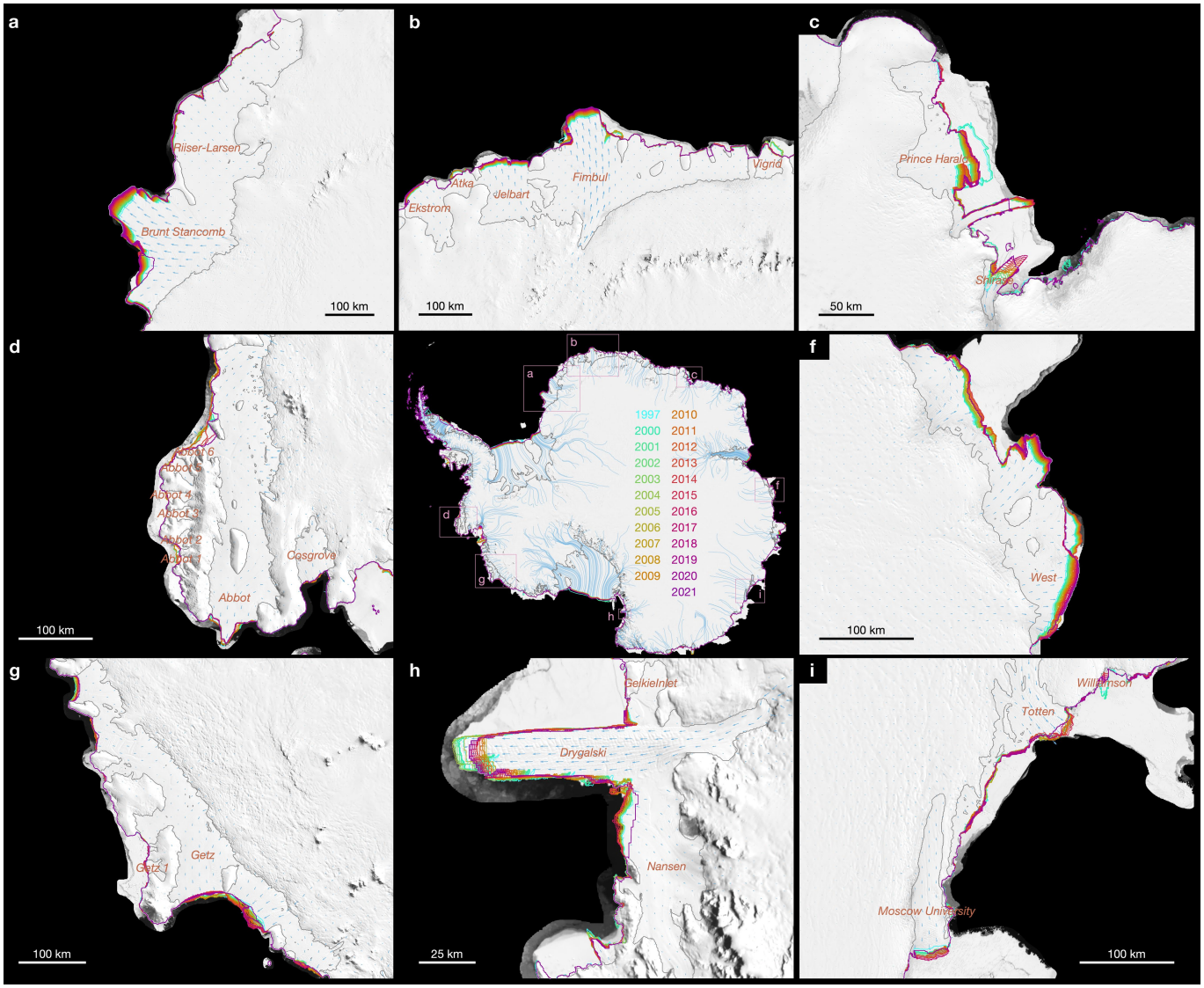


**Extended Data Fig. 1 | Antarctic coastal change since 1997 (continued).** The coastline evolution over the past quarter of a century, shown for selected regions that do not appear in Fig. 1.

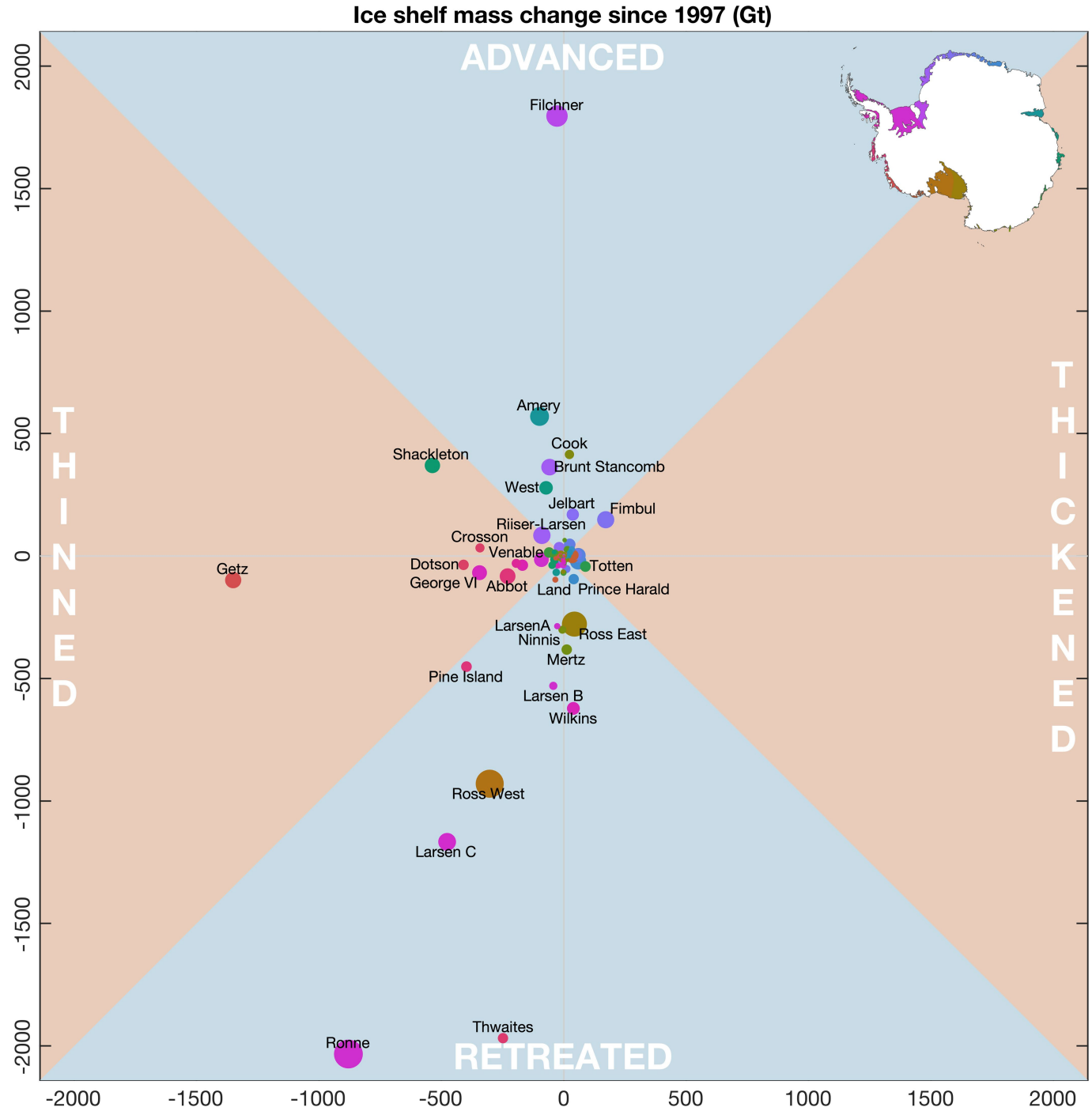


**Extended Data Fig. 2 | Ice shelf mass change since 1997.** The mass imbalance of ice shelves in the blue triangles is dominated by coastal processes, while the balance of only a few ice shelves, mostly located in the Amundsen Sea Embayment, are dominated by thinning. Marker colour corresponds to the central longitude of each ice shelf, and marker area scales with ice-shelf area.

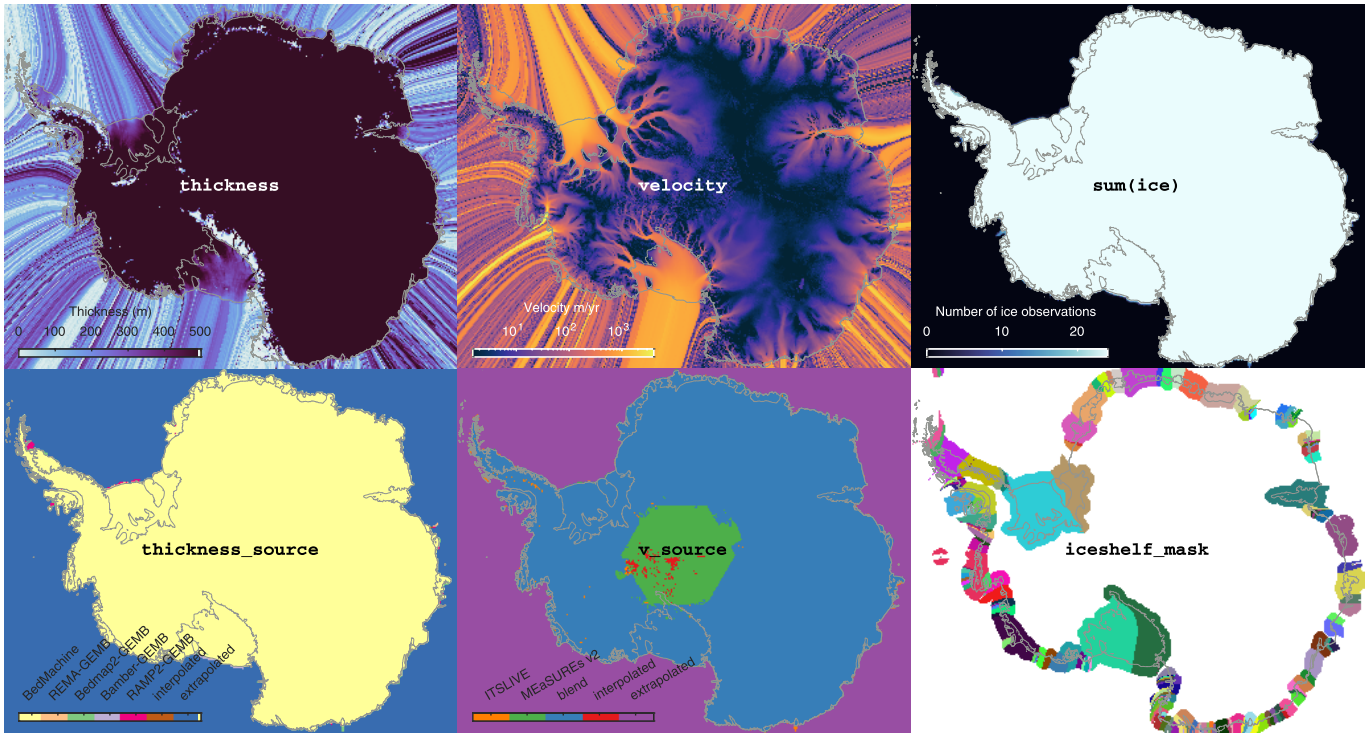


**Extended Data Fig. 3 | Gridded datasets.** To quantify changes at the ice-sheet margins, where publicly available velocity and thickness datasets may not reach the maximum observed extents of the ice sheet, we combine all available data, then extrapolate thickness, velocity, and a mask of ice-shelf names in the direction of ice flow. Although the resulting grids fill the entire map, we only use thickness and velocity data close to the Antarctic periphery, wherever ice has been observed in at least one of the 24 mappings since 1997.

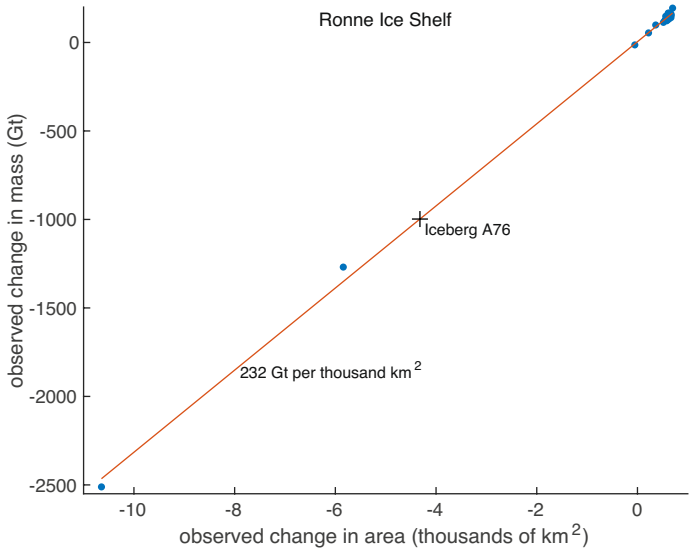


**Extended Data Fig. 4 | Iceberg A76 mass estimation.** Weeks after our March 2021 annual pan-Antarctic coastline mapping, the Ronne Ice Shelf calved the 4320 $km^2$ iceberg A76. By considering changes in area and mass that have occurred between each of our 24 consecutive mappings, we estimate that iceberg A76 took 1,002 Gt of ice from Ronne Ice Shelf.

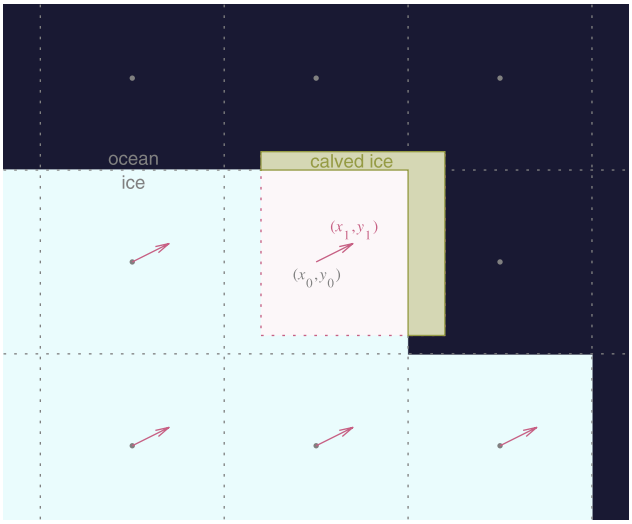


**Extended Data Fig. 5 | Steady-state calving-flux calculation.** To obtain steady-state calving flux, we calculate pixel centre locations $(x_1,y_1)$ of a 240-m resolution grid after one year of ice displacement. We use $(x_1,y_1)$ as query points to linearly interpolate a binary ice mask, which gives the fraction of each grid cell that is still within the initial mask after a year of displacement. Calving flux is calculated by multiplying the fraction of ice that has calved after a year of displacement by the area, thickness, and density of ice in each grid cell.

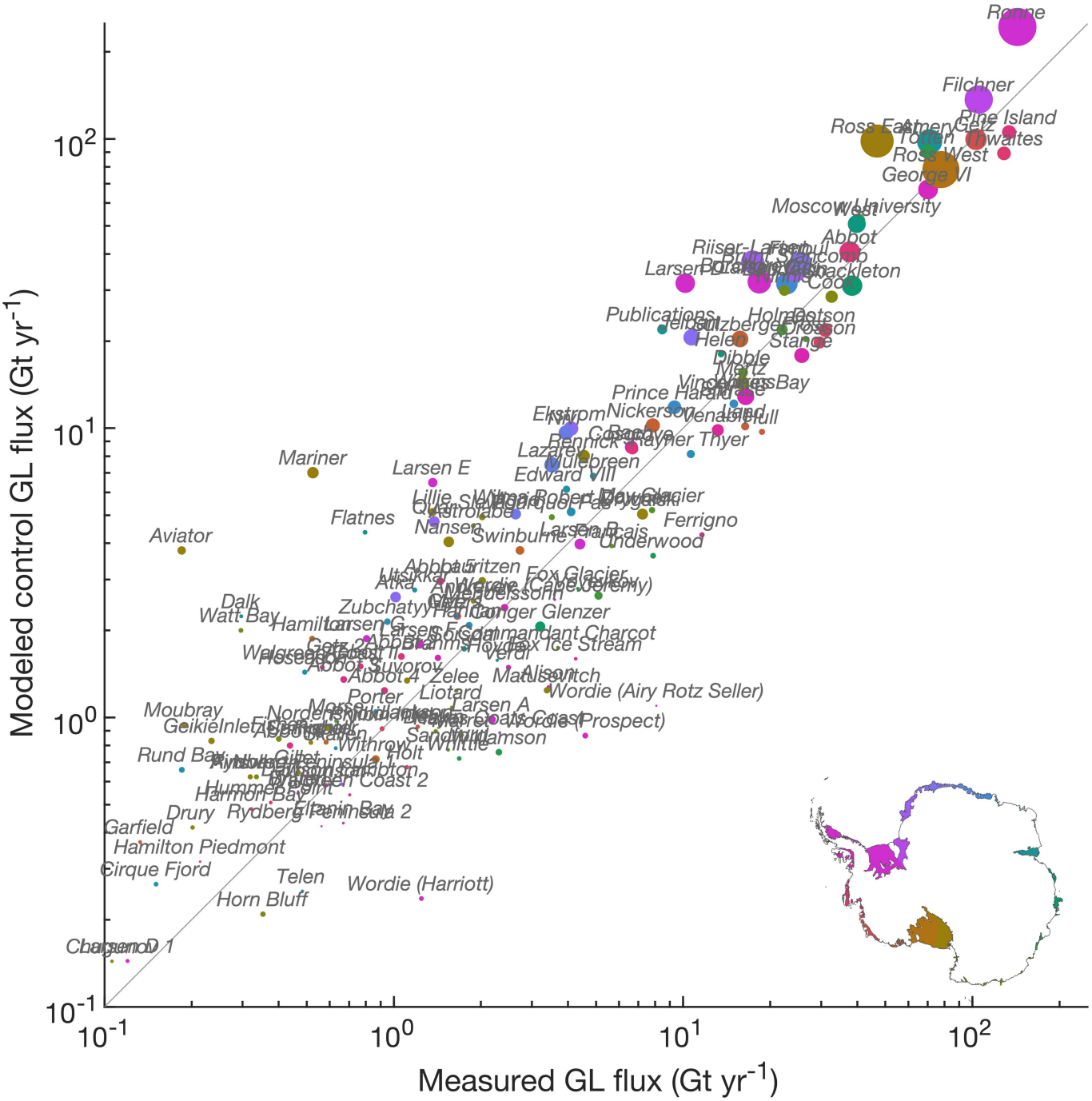


**Extended Data Fig. 6 | Measured and modelled grounding-line flux.** All sensitivity measurements described in this manuscript present grounding-line-flux measurements relative to the control values shown here. Marker area scales with ice-shelf area and marker corresponds to the central longitude of each ice shelf.

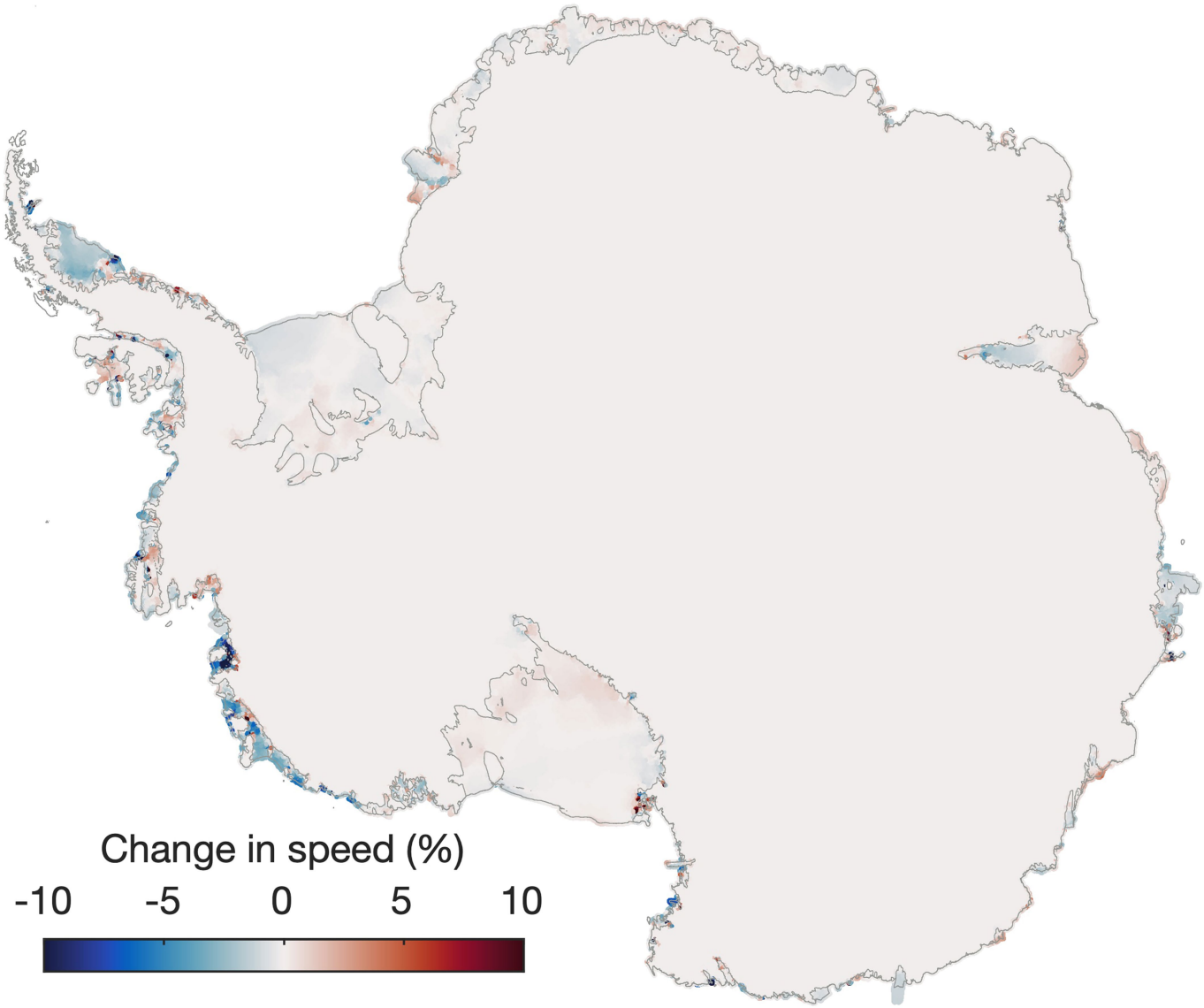


**Extended Data Fig. 7 | Comparison to ref. [38].** To help validate the ice-sheet model, we replicate the results from Fig. S12 of ref. [38]. This figure shows the instantaneous velocity response resulting from step change in thickness from 2010 to 2017 observations.